RSC Advances

ROYAL SOCIETY OF CHEMISTRY

www.rsc.org/advances

Significant Enhancement of the Electroactive β Phase of PVDF by Incorporating Hydrothermally Synthesized Copper Oxide Nanoparticles

Biplab Dutta[1], Epsita Kar[1], Navonil Bose[1,2], Sampad Mukherjee[1*]

[1] Department of Physics, Indian Institute of Engineering Science and Technology, Shibpur, Howrah-711103, India

[2] Department of Physics, Government Engineering College, Ramgarh-829122, Jharkhand, India

*smukherjee.besu@gmail.com, Ph- +919433579392

Abstract

The influence of copper oxide nanoparticles (CONPs) on the polymorphism of the poly(vinylidene fluoride) (PVDF) is systematically investigated in this work. Copper oxide nanoparticles having average diameter of 60 nm were synthesized by simple, cost effective, environmentally benign modified hydrothermal method, hence a series of copper oxide nanoparticles incorporated flexible, self -standing PVDF films were prepared by solution casting technique. The impact of CONPs loading on the structural and morphological properties of the PVDF were studied by X-ray diffraction, scanning electron microscopy and Fourier transform infrared spectroscopy techniques. Thermal properties of the sample were investigated by differential thermal analysis, thermogravimetric analysis and differential scanning calorimetry techniques. Incorporation of CONPs leads to the faster crystallization and thereby promoting the formation of electroactive β-phase enriched PVDF films. Strong interfacial interaction between the negatively charged nanoparticles surface and positively charged $-CH_2$ dipoles of the PVDF leads to the significant enhancement of electroactive β phase. 5wt% CONPs/PVDF composites film exhibits maximum β phase fraction of 90% due to the highest interfacial area between the well dispersed nanoparticles surface and the polymer.

Keywords: PVDF; Copper oxide nanoparticles; Hydrothermal method; β phase; Structural Properties, Thermal Properties.

1. Introduction

Recently electroactive polymers have attracted much attention due to their various potential applications in energy harvesting, sensors, actuators and in the biomedical fields [1-4]. In the midst of few polymers showing the piezoelectric, pyroelectric and ferroelectric properties, such as Nylon-11, poly(lactic-co-glycolic acid) (PLGA) and polylacticacid (PLLA) [5-9], poly(vinylidene fluoride) (PVDF) and its copolymers have the greatest versatile electroactive properties. Therefore PVDF and its copolymers like poly(vinylidene fluoride-trifluoroethylene) [P(VDF-TrFE)], poly(vinylidene fluoride-hexafluoropropylene) [P(VDF-HFP)] are emerging as popular polymers of choice for growing number of potential applications [10-13]. Poly(vinylidene fluoride) ($[–CH_2–CF_2–]_n$), a flexible, cost effective fluoropolymer has achieved much interest due to its wide range of significant applications in piezoelectric nanogenerator, high charge storage capacitors, electro-striction for artificial muscles, magneto-striction, non-volatile memories in microelectronics, thin film transistors, pulsed lasers [1,10-13]. PVDF is a semicrystalline polymer having five different crystalline phases, c.a. α, β, γ, δ and ε [14]. Among all of these phases the non-polar α phase is the most common and thermodynamically stable state at ambient temperature and pressure. On the other hand β and γ phases are the polar phases of the PVDF. The α phases possess monoclinic unit cell structure with TGTG´(T- trans, G- gauche+, G´- gauche) dihedral conformation. Whereas, β and γ phases contain orthorhombic unit cell structure with TTT (all trans) and 3TG3TG´ conformation respectively [14-17]. However β phase acquires more importance over the other phases due to its better piezoelectric, ferroelectric and pyroelectric properties [8-9,11,24]. Thus, many research works regarding the enhancement of the electroactive β-phase content in PVDF have been reported for various applications of the particular polymer [8-9, 14, 18-19]. Different techniques including uniaxial or biaxial drawing of

α-PVDF films, simultaneous poling, stretching and quenching the α-PVDF films, melting crystallization of α-PVDF under high pressure, supercritical carbon dioxide technique, electro-spinning method are used to achieve higher β-phase content in PVDF [9]. The enhancement of the electroactive β-phase fraction in PVDF matrix can also be achieved by incorporation of various sub-micron or nanosized filler materials including metal, metal oxide, clays, ceramics, semiconductor oxide, carbon nanotubes, graphene, inorganic salts, ferrites [8,9,11,18-26]. Since the size of fillers are in nano-dimension, the interfacial interactions between the nanofillers and polymer matrix increase significantly due to the high surface-to-volume ratio of the nanofillers, thus the addition of small amount of nanofillers results in improved physicochemical properties of the polymer without compromising the polymer flexibility. Gold [18], silver [19], iron oxide and cobalt oxide [24] nanomaterials are used to enhance the electroactive β phase content in PVDF. It is well known that usage of metal and metal oxide nanoparticles can also significantly improve mechanical, electrical and magnetic properties of polymeric composite films without losing the flexibility of the composite films [18, 20-21,25]. Amid the different metal oxides nanoparticles fillers, copper oxide nanoparticle has gained a paramount importance due to its key role on the enhancement of the electrical properties of PVDF [20,25]. Significant enhancement of dielectric constant ($\varepsilon' \sim 10^3$) of copper oxide/PVDF nanocomposite films has been previously reported [20]. It will be interesting to study the effect of the incorporation of comparatively cost effective copper oxide nanoparticles (CONPs) on the nucleation of the electroactive β phase in PVDF as well as to study the structural and thermal properties of the copper oxide/PVDF nanocomposite films, which are not reported till date.

This present work deals with the synthesis of copper oxide nanoparticles by modified hydrothermal method. Hydrothermally synthesized copper oxide nanoparticles are incorporated

in the PVDF matrix. Detailed analyses of the structural and thermal properties of the CONPs loaded PVDF films have been included in this study. The effect of the copper oxide nanoparticles on the nucleation of the electroactive β phase in PVDF along with the reason behind the significant improvement of the β phase fraction has also been discussed from the physicochemical point of view.

2. Experimental:

2.1 Materials:

Poly(vinylidene fluoride) (PVDF) pallets (Mw = 27500 gm/mol) were obtained from Sigma Aldrich, USA. Dry N,N, dimethylformamide (DMF; Merck, India), copper(II) Sulphate Pentahydrate ($CuSO_4$, $5H_2O$, Mw =249.685gm/mol; Merck, India), sodium hydroxide (NaOH; Merck, India) and ethyl alcohol (C_2H_6O; Merck, India) were used in this work. All the materials were used in the experiments without further purification.

2.2 Synthesis of copper oxide nanoparticles:

The copper oxide nanoparticles were synthesized by modified hydrothermal method [27]. In this typical procedure initially a 0.1M solution of $CuSO_4$, $5H_2O$ was prepared in distilled water. A 1M NaOH solution was then added drop by drop to the solution of $CuSO_4$, $5H_2O$ under vigorous stirring until the pH of the resultant solution becomes 13. After that, the solution was transferred to a stainless steel autoclave and sealed properly. The autoclave was heated in a furnace at a temperature of 110℃ for 18 hours. Hence the autoclave was set for natural cooling. After cooling down to room temperature (30°C), the obtained solution was centrifuged (4000 rpm) for 30 minutes. The as obtained product was properly washed for several times using distilled water and ethyl alcohol to remove the residual impurities. Finally, the solution was dried to obtain the

resultant powder and the powder sample was then kept in a vacuum desiccator for the complete reduction of the residual solvent contained in the powder.

2.3 Synthesis of copper oxide loaded PVDF nanocomposite films:

The copper oxide nanoparticles loaded PVDF films were synthesized by the simple solution casting method. In this typical synthesis procedure, 500mg of PVDF was dissolved in 20 ml DMF under vigorous stirring at 60°C and the complete dissolution of PVDF in DMF was achieved. Then a certain weight percent (1-5 wt%) of the as synthesized copper oxide nanoparticles were added to the solution of PVDF and vigorously stirred for 16 hours followed by a 30 min sonication to obtain a homogeneous mixture. The nanocomposite films were prepared by casting the mixture in a properly cleaned and dried Petri dish, and the solvent was evaporated at 90°C. Neat PVDF films were also prepared following the same procedure along with the loaded PVDF films. 1wt%, 3wt% and 5wt% copper oxide nanoparticles loaded PVDF films are prepared in this work which are named as PCO1, PCO3 and PCO5 respectively. Prepared Neat PVDF is named as P0.

2.4 Characterization Methods:

The structural properties of the as synthesized CONPs and composite films were studied by X-ray diffractometer (Bruker-D8) with Cu-Kα radiation (wavelength 1.541 A^0) using Bragg-Brentano goniometer geometry and θ-2θ mechanism. The XRD patterns of all the samples are recorded with scan speed of 0.3 sec per step and under an operating voltage of 40kV with 2θ varying from 10 to 50^0.

Absorption spectra of the as synthesized CONPs and CONPs loaded PVDF films were recorded by UV-Visible spectrophotometer (Jasco V-630 Spectrophotometer) in the wavelength range 200-1100 nm.

The surface morphology of the nanoparticles and the as synthesized copper oxide nanoparticles doped PVDF films were studied by using field emission scanning electron microscopy (FESEM) (Quanta, FEG 250) technique. Energy dispersive X-ray spectroscopy (EDAX) of the samples was also carried out in the same FESEM instrument. Structure, shape and size distribution of the as synthesized copper oxide nanoparticles were studied by transmission electron microscope (TEM) using FEI.TECHNAI.T-20 G2 SUPERTWIN (200 kV) instrument.

Vibrational spectra for all the samples were recorded at room temperature by the Fourier transform infrared (FTIR) spectroscope (Jasco FT/IR-460 PLUS) having resolution of $1cm^{-1}$. The fraction of β phase F(β) in the as synthesized nanocomposites films is calculated from the FTIR spectra using Lambert-Beer Law as given by[14],

$$F(\beta) = \frac{A_\beta}{\left(\frac{K_\beta}{K_\alpha}\right)A_\alpha + A_\beta} \qquad (1)$$

Where A_α and $A_\beta$are the absorbance at 764 cm^{-1} and 840 cm^{-1} respectively. K_α(6.1×10^4 cm^2 mol^{-1} and K_β (7.7×10^4 cm^2 mol^{-1}) are the absorption coefficients at $764cm^{-1}$ and $840cm^{-1}$ respectively [14].

Differential thermal analysis (DTA) and thermogravimetric analysis (TGA) were performed by using TGA/SDTA851 Mettler Toledo apparatus in air atmosphere at a heating rate of 10^0C/min. The crystallization and melting behavior of the pure as well as copper oxide nanoparticles loaded PVDF films were analyzed using a differential scanning calorimeter (DSC-60, Shimadzu (Asia Pacific) Pte. Ltd, Singapore). All the samples were heated from 30^0C to 200 ^{0}C at a rate of 10^0C min^{-1}in nitrogen gas atmosphere. The degree of crystallinity (X_c) of the samples are calculated using the following equation [28]:

$$X_c = \Delta H_c / \Delta H_{100\%} \qquad (2)$$

Where, ΔH_c is the enthalpy of crystallization and $\Delta H_{100\%}$ is the melting enthalpy of 100% crystalline PVDF with a value 104.6 Jg^{-1}.

3. Result and discussion:

3.1 Copper Oxide nanoparticles

X-ray diffraction analysis (XRD). Fig.1 illustrates the X-ray diffraction (XRD) pattern of the as synthesized copper oxide nanoparticles, which reveals the well crystalline nature of the sample. The diffraction peaks positioned at 2θ values 35.3°, 38.5^0, 52.3^0, 61.2^0, 66.0^0, 67.9^0 and $71.7^0$are corresponding to the ($\bar{1}11$), (111), (020), ($\bar{1}13$), ($\bar{3}11$), (113) and (311) planes of the crystalline phase of monoclinic cupric oxide (CuO) in accordance with the JCPDS no. 41-0254 (a=4.685 Å, b=3.423 Å, c=5.132 Å, space group: C12/c1). The peaks positioned at2θ values 13.7^0, 16.8^0, 21.3^0, 27.6^0, $32.3^0$are assigned to the (110), (111), (220) and (311) planes of crystalline phase of cubic cuprous oxide (Cu_2O) (JCPDS no. 34-1354, a=4.217 A^0, space group: $Pn\bar{3}m$). The XRD analysis infers that the as synthesized copper oxide nanoparticles are in the mixed crystalline phases of CuO and Cu_2O with a dominating fraction of CuO phase.

Electron microscopy analyses. The field effect scanning electron micrograph (FESEM) of the as synthesized copper oxide nanoparticles is shown in Fig.2a. Inset of the figure shows the particle size distribution curve. The figure shows that the platelet like shaped particles with an average size ~170 nm is stacked together. Fig.2b shows the transmission electron microscopic (TEM) micrograph of the as synthesized copper oxide nanoparticles. The size distribution curve obtained from the TEM micrograph is shown in the inset of the Fig.2b. The figure shows that the copper oxide nanoparticles possess hexagonal like structure with well-defined boundaries. As seen from the size distribution curve the average diagonal length of these nanoparticles is ~ 60 nm. Fig. 2c shows the selected area electron diffraction (SAED) pattern of the copper oxide

nanoparticles. Single crystalline nature of the nanoparticles is evident from the 'Dot' patterned SAED result. The measured d-spacing values from the SAED pattern are 0.116 nm, 0.150 nm, 0.148 nm which confirm that the synthesized copper oxide sample is in mixed crystalline phase of CuO and Cu_2O as the d-spacing values are in good agreement with that of the CuO and Cu_2O crystals (JCPDS no. 34-1354 and 35-1091). Fig. 2d exhibits the EDAX result of the hydrothermally synthesized sample, which shows the only presence of the characteristic peaks corresponding to O and Cu element confirming the high purity of the synthesized copper oxide nanoparticles.

UV-Visible Spectroscopy. The UV-Visible absorption spectrum of the as synthesized copper oxide nanoparticles as shown in Fig.3shows a strong absorption peak positioned at wavelength 258 nm.The presence of this absorption peak can be attributed to the existence of cuprous oxide (Cu_2O) phase of the CONPs. Similar, existence of absorption peak for cuprous oxide has already been reported by Y. Abboud et.al [29]. In addition to that, another broad absorption peak centered ~ 650nm can also be seen from the Fig.3.The presence of cupric oxide (CuO) phase in the synthesized CONPs is responsible for this broad absorption peak [29]. Thus the UV-Visible absorption spectrum of the copper oxide nanoparticles also confirms the co-existence of both the CuO and Cu_2O phases of CONPs.

3.2 Copper oxide loaded PVDF nanocomposite films

X-ray diffraction analysis (XRD). X-ray diffraction (XRD) spectroscopy is used to analyze the polymorphism of neat PVDF and copper oxide nanoparticles loaded PVDF films. Fig.4a shows the XRD pattern of the neat PVDF (P0) and PVDF films loaded with different concentration of CONPs c.a. PCO1, PCO3 and PCO5. As seen from the figure, the diffraction pattern of neat PVDF reveals the semi-crystalline nature of the polymer. The peaks positioned at $2\theta = 17.5^{\circ}$

(100), 18.2º (020), 19.8º (021), and 26.6º ((201), (310)) of the neat PVDF can be assigned to the nonpolar α phase of PVDF [14,23]. A well recognizable peak for the loaded PVDF films positioned at 2θ value 35.3° ($\bar{1}11$) can be clearly indexed to the monoclinic CuO phase (JCPDS-41-0254) of CONPs, whereas peaks at 2θ values 13.57° (110), 22.54° (200) and 33.17° (311) can be assigned to the cubic Cu_2O phase (JCPDS-34-1354) of CONPs. The occurrence of these peaks attributed to the different phases of CONPs infers the successful incorporation of CONPs in PVDF matrix. The XRD patterns also show that with increasing loading fraction of nanoparticles the intensity of the peaks corresponding to the α phase of PVDF (positioned at 17.5º, 18.2º, 19.8º and 26.6º) decreases gradually. However, a new peak positioned around 2θ = 20.6º ((020), (101)) appears in the copper oxide nanoparticles loaded PVDF films, which is the characteristic peak of the β phase PVDF [14,23]. A closer observation of the XRD pattern reveals that for the sample PCO5, intensity of the peak positioned at 26.6º corresponding to the nonpolar α phase of PVDF is almost completely diminished , whereas the relative intensity of the peak positioned at 2θ = 20.6 (characteristic peak of β phase PVDF) becomes maximum. It can be also seen from the XRD pattern that a peak positioned at 2θ = 38.9° (211) corresponding to the γ phase of PVDF [14,23] is present for the neat as well as loaded PVDF films. The ratio ($I_{20.6^\circ}$/ $I_{18.2^\circ}$) manifests the measurement of α and β phase content in the neat PVDF and CONPs incorporated nanocomposite films, where $I_{20.6^\circ}$ and $I_{18.2^\circ}$ are the intensities of the peaks positioned at 20.6°(characteristic peak for β phase) and 18.2° (characteristic peak for α phase) respectively. Fig.4b represents the content dependence of the ratio ($I_{20.6^\circ}$/ $I_{18.2^\circ}$). For the neat PVDF film the ratio is about 0.93 and this ratio is increased with the increasing weight fraction of the CONPs in the PVDF matrix. The maximum value of the ratio is c.a. 12.05 obtained for the sample PCO5 (5 wt%). Thus, as a whole the XRD patterns of loaded PVDF films confirm that

the incorporation of the CONPs results in a phase transformation from the α phase to the electroactive β phase of PVDF.

Field emission scanning electron microscopy (FESEM). Fig.5 exhibits the FESEM micrograph of the neat PVDF. The surface morphology of the neat PVDF shows that the matrix possesses a highly compact and uniform morphology. In addition to that well-recognizable (marked by red circle) spherulite with diameter ~ 8μm is evident from the FESEM micrograph. In Fig.6a, the low magnification FESEM micrograph of the sample PCO5 shows the surface morphology of the film, which reveals a uniform distribution of the spherulites (marked as red circles in the figure) having diameter of 2-3μm throughout the surface of the composite film.

The uniform distribution of the spherulites confirms the well, homogeneous dispersion of copper oxide nanoparticles in the PVDF matrix. The smaller size of the spherulites for the sample PCO5 in comparison to that of the neat PVDF represents the faster nucleation kinetics in CONPs/PVDF composite films [28] due to the presence of additional CONPs nucleation centers and the enhancement of the β phase fraction may be achieved in the composite film due to the existence of these large number of favorable nucleation centers [28]. Again the presence of the added CONPs in the PVDF can be clearly seen from the high magnification FESEM micrograph of the sample PCO5 in Fig.6b. It is evident from the figure that the surface of PVDF film is completely modified with the addition of CONPs. Impinging of spherulites (marked by red straight lines) is observed in the figure due to the faster kinetics in the presence of CONPs. Thus the FESEM images for both the neat and the composite films support the enhancement of the electroactive β phase due to the incorporation of the CONPs which is in consistence with the result obtained from the X-ray diffraction pattern of the samples. Fig. 6c represents the EDAX result of the CONPs loaded PVDF film (PCO5). The figure shows the presence of characteristic peaks

corresponding to Cu, O, C and F elements where C and F are the polymeric components of the PVDF matrix, and Cu, O are the components of CONPs as previously showed in Fig.2d. Hence the presence of copper oxide in PVDF is further confirmed by the EDAX result.

UV-Visible Spectroscopy. Fig. 7 shows the UV-Visible absorbance spectra of the neat PVDF along with the CONPs loaded PVDF films (PCO1, PCO3 and PCO5) within the range 200 nm-1100 nm. The UV-Visible spectrum of neat PVDF infers that the neat PVDF is transparent in the higher wavelength region starting from visible region. However, the presence of a well -defined absorption peak positioned at a wavelength ~270 nm for the CONPs loaded PVDF films is evident from the figure. It is worthwhile to mention here that the absorption peak for the CONPs is positioned at wavelength ~258 nm as seen from the Fig.3.Thus, the UV-Visible spectra for the loaded PVDF films revels that the absorption peak for the CONPs is being shifted in the presence of the host polymer matrix. This observation may be explained by the presence of the host polymer matrix surrounding the CONPs, which may affect the electronic transition in valence band and conduction band in copper oxide nanoparticles due to the strong electrostatic interaction of the CONPs filler with the polymer matrix [9].The figure also shows that the intensity of the absorption peaks is increased with the increasing loading fraction of the copper oxide nanoparticles in PVDF matrix which may be attributed to the homogeneous dispersion of the nanoparticles in PVDF matrix [9].

Fourier Transform Infrared Spectroscopy. Fig. 8a shows the as-recorded Fourier transform infrared (FTIR) absorption spectra of the neat PVDF and CONPs loaded PVDF films c.a. PCO1, PCO3, PCO5. The FTIR spectrum of the neat PVDF shows characteristic peaks at 488 cm^{-1} (CF_2 waging), 532 cm^{-1} (CF_2 bending), 615 cm^{-1} and 764 cm^{-1} (CF_2 bending and skeletal bending), 796 cm^{-1} and 976 cm^{-1} (CH_2 rocking) corresponding to the IR bands of nonpolar α phase of

PVDF [8] . Two small peaks corresponding to β phase of PVDF [8] are also observed at 510 cm^{-1} (CF_2 stretching) and 840 cm^{-1} (CH_2 rocking, CF_2 stretching and skeletal C–C stretching) for neat PVDF. It can be clearly seen from the figure that all the characteristic absorption bands corresponding to nonpolar α phase of PVDF are gradually diminished with increasing loading fraction of CONPs in PVDF. Moreover relative intensities of the peaks corresponding to the β phase increase with increasing CONPs loading. A closer observation shows that for the sample PCO5 all the peaks corresponding to α phase are almost completely disappeared, only the characteristic absorbance bands assigned to polar β phase are dominantly appeared at 510 cm^{-1}, 600 cm^{-1} (CF_2 waging), 840 cm^{-1} [8]. Therefore, the FTIR results strongly indicate the α to β phase transformation of PVDF with the loading of the CONPs in the PVDF matrix. To have a quantitative study of the phase transformation for the CONPs loaded PVDF films, fraction of β phase (F(β)) is calculated for the nanocomposite films using equation (1). The variation of F(β) with CONPs content is shown in Fig.8b. A rapid increment in F(β) value for the sample PCO1 is evident from the figure, then the F(β) increases almost linearly with the increasing filler content of CONPs. The maximum β phase nucleation is occurred for the 5wt% CONPs loading, which is about ~ 90 %. This enhancement of β phase fraction with the filler loading may be readily explained by the interaction between the filler and the polymer matrix. At low filler content the amount of interfacial area between the polymer and the CONPs is low, while, interfacial area increases with the increasing content of CONPs in PVDF as the CONPs are homogeneously dispersed in the polymer matrix. As a consequence, the number of aligned chains having 'all trans' conformation increases resulting in an increase in the β phase fraction. The variation of F(β) also suggests that the most intimate interaction between the polymer and the CONPs occurs at 5 wt % loading of the filler.

Thermal Properties. Thermal properties of neat PVDF and CONPs loaded PVDF films have been investigated by TG-DTA techniques. Fig. 9a shows the DTA results of the neat PVDF and the PVDF nanocomposite films in the temperature range 30°C to 600°C. Enlarged view of the DTA result in the temperature range 140°C to 170°C is shown in the inset of the same figure. The figure reveals the presence of an endothermic peak position around 155.8°C for the neat PVDF, which is attributed to the melting temperature of the neat PVDF [8,21]. It can also be seen from the figure that, with the increasing loading fraction (1-5 wt%) of the nano-fillers (CONPs) the melting temperature of the composite films is increased in comparison to that of the neat PVDF film. The maximum shift (3°C) in melting temperature is observed for the sample PCO5, similar increase in melting temperature (5-7 °C) with the loading of the nickel particles (0 to 2.0 wt%) in PVDF matrix was previously reported by S.M. Levedev et.al. [21]. This increase in the melting temperature may be attributed to the change in degree of crystallinity and homogeneity in sub-molecular structure of the nanocomposite film compared to the neat films [8,21].The presence of copper oxide nanoparticles in PVDF matrix is responsible for such changes in the melting temperature of the nanocomposite films. The increment in melting temperature of the nanocomposite film also confirms the formation of the electroactive β phase in the nanocomposite films [8,21]. About 2° C shift of the main exothermic peak for the sample PCO5 in comparison to the neat PVDF film can be observed from the DTA curve (Fig.9a), which infers the good thermal stability of the nanocomposite films. Fig. 9b shows the TGA analysis of the neat, PCO1 and PCO5 films. The figure shows a significant, step like weight loss, which starts around 450°C and continues up to 500°C for all the samples. This weight loss is related to the decomposition of the films by stripping mechanism, during which hydrogen fluoride (HF) gas is released from the samples. During this degradation process, about 40 % of

hydrogen fluoride gas has found to be released in this temperature range from the neat film as calculated from the TGA curve [8]. TGA curves in Fig.9b also confirm the fair enhancement in decomposition temperature of the nanocomposites films, leading to the improved thermal stability of the films. Inset of the Fig.9b shows the TGA curve of the synthesized neat copper oxide nanoparticles. Copper oxide nanoparticles powder has almost no weight loss in the temperature region 30-600 °C except for the loss of water due to the formation of only metal oxide [30].

To determine the kinetic parameters for the thermal degradation of the nanocomposite films the Coast-Redfern equation [31] is usually used, which is as follows:

$$\ln\left[\frac{-\ln(1-\alpha_d)}{T^2}\right] = -\frac{E_d}{RT} + \ln\left(\frac{AR}{BE_d}\right) \qquad (3)$$

where E_d is the activation energy, R is the universal gas constant (8.814 J/mol.K), A is the pre-exponential factor, B is the heating rate (10°C/min), T is the degradation temperature (K) and α_d is the degree of conversion. Degree of conversion (α_d) is denoted as the kinetic of conversion of the polymer to volatile decomposition product. At a given temperature α_d is defined by [31],

$$\alpha_d = \frac{m_i - m_T}{m_i - m_f} \qquad (4)$$

where m_i, m_T, and m_f are the initial sample weight, weight of the sample at temperature T and weight of the final sample respectively. In this work the kinetic parameters of thermal decomposition for the samples P0, PCO1 and PCO5 are calculated around the maximum degradation temperature (where the maximum weight loss has occurred). In Fig.10a-c, the plot of $\ln\left[\frac{-\ln(1-\alpha_d)}{T^2}\right]$ against 1/T (K^{-1}) for the sample P0, PCO1and PCO5 gives linear curves with negative slope. From the slope of the curves, the value of the decomposition activation energy

(E_d) of the neat and nanocomposite films has been calculated. The calculated values of the decomposition activation energy and the corresponding values of the regression coefficient (R^2) for the neat and loaded films are given in Table-1. In this context it should be noted that the value of the regression factor (R^2) is close to unity for all of the samples. The activation energy of the loaded films is higher than that of the neat PVDF films, which infers that the loading of the CONPs in the PVDF matrix increases the thermal stability of the nanocomposite films in comparison to the neat PVDF. This enhancement in thermal stability for the nanocomposites films is also in fair agreement with the DTA-TGA results. Maximum value of the activation energy is obtained for sample PCO5, which is 654.22 K Joule/mole. Similar increase in thermal stability by incorporating$WO_3.H_2O$ nanoparticles in the PVDF matrix has been reported by Thakur et al. [9].

The interface between the polymer and nanofillers plays key role in determining the final properties of the nanocomposite films. Form the TGA results, the nanofiller/polymer interface region (m_I) of the CONPs/PVDF composite was obtained by using the following equation [37],

$$m_I = \frac{m(x)_{I0} - m_{I0}}{m_{I0}} \times 100\% \qquad (5)$$

where, m_{I0} is the mass of the pristine PVDF at the temperature at which the mass loss rate is maximum and $m(x)_{I0}$ is the mass of the composite containing a given wt% of nanoparticles that has not degraded at the same temperature. Fig.11 shows the variation of the mass fraction (m_I) of the polymer located at the interface with the loading fraction (1-5%) of the CONPs nanofiler in PVDF. The figure shows a rapid increment in m_I value for the sample PCO1, then the m_I increases almost linearly with the increasing loading fraction of CONPs. The maximum value of m_I (20%) is obtained for the sample PCO5 (5 wt% CONPs loaded PVDF. As a result the number of particles interacting with the polymer matrix is highest for PCO5. Higher m_I value reflects the

increment in interaction between the partially positive CH_2 bonds of the PVDF chains and the electrostatically negative charged CONPs, which again promotes the β phase nucleation. This fact is also supported by the FTIR, XRD results which show the highest β phase fraction is obtained for the sample PCO5. It is worthwhile to mention here that the CONPs are not agglomerated in polymer matrix up to filler loading of 5 wt%, rather they are discretely distributed in the polymer matrix leading to a higher m_I value at higher filler loading fraction.

Thermal properties and polymorphism of the composites are also studied using DSC. Fig.12a-c show the DSC heating cycles of the samples P0, PCO1 and PCO5 respectively. To get a deeper insight into the coexistence of different PVDF phases in composite films, DSC curves are fitted with multiple Gaussian functions corresponding to the α, β and γ phase PVDF. The multi-peak fitted DSC heating curves reveal the presence of three distinguishable peaks inferring the coexistence of α, β and γ phases in neat as well as PVDF nanocomposite films. The melting temperature for all the samples corresponding to the three different phases are shown in Table 2. Figures show that the relative intensity and the area under the peak related to the melting temperature of β phase increase with the increasing filler concentration of CONPs. On the other hand, the intensity and the area under the curve assigned to the α-PVDF diminishes significantly with the increasing loading fraction of CONPs in PVDF matrix. This observation can be explained by the increment in the β - PVDF nucleation in expense of the reduction in α – PVDF fraction in the composite films. Transformation from α to β polymorph occurs due to the incorporation of CONPs. It can be seen from the Fig.12c that for the sample PCO5 the relative intensity of the peak related to β phase PVDF is maximum, while the peak related to α phase PVDF is almost completely diminished. It is worthwhile to mention here that the XRD and FTIR analyses of the neat and PVDF nanocomposite films also validate the presence of maximum β

phase fraction in the sample PCO5. The DSC cooling cycles for neat PVDF and copper oxide nanoparticles loaded PVDF films are shown in Fig.13. Though multiple endothermic peaks can be seen from the heating cycle of the neat and CONPs loaded PVDF films, but the cooling cycle of the samples show a single exothermic peak, this infers the existence of polymorphs in the films. However, a single exothermic peak is obtained for cooling cycle as after the first heating cycle in DSC, the processing history is erased. The single exothermic peak present in the DSC cooling cycle is attributed to the crystallization temperature (T_c) of the neat and loaded PVDF films. Crystallization temperature for the CONPs incorporated PVDF films is higher than of neat PVDF as observed from the Fig.13 and it increases with the increasing content of CONPs in the PVDF matrix. This observation is expected as the incorporated copper oxide nanoparticles act as the nucleating agent in the PVDF matrix, thereby influencing the crystallization temperature. For the sample PCO5 crystallization temperature is increased ~ 2 °C in comparison to that of the neat PVDF. This indicates that the addition of well dispersed CONPs as the nucleating agent lowers the free energy barrier of nucleation, thus accelerating the crystallization of PVDF, manifested in a higher crystallization temperature for nanocomposites films [28]. The faster nucleation kinetics is also evident from the FESEM micrograph of PCO5 (Fig.6a) where smaller spherulites in comparison to neat PVDF are observed. DSC thermographs are also used to obtain the enthalpy of crystallization (ΔH_c J/g) and the degree of crystallinity (X_c) of the neat PVDF as well as CONPs/PVDF composites films. The degree of crystallinity of the samples is calculated using the equation (2). Crystallization temperatures (T_c), enthalpy of crystallization (ΔH_c), and the degree of crystallinity (X_c) for the samples P0, PCO1 and PCO5 are reported in Table 3. The crystallinity decreases with addition of CONPs in PVDF matrix and PCO5 shows minimum value of X_c. As evident from XRD and FTIR results, neat PVDF contains three phases α, β and γ,

but for the sample PCO5 the α- phase of PVDF is almost completely diminished and only present dominant crystalline phase is β-PVDF resulting reduction in overall crystallinity of the composite films. This indicates the intimate interaction of CONPs with PVDF, thus strong influence of nanoparticles on structural modification of PVDF matrix.

3.3 Mechanism of electroactive β phase nucleation. The results obtained from the XRD, FTIR, and thermal studies of the nanocomposites films confirm that the incorporation of copper oxide nanoparticles in the PVDF matrix leads to an increase in electroactive β phase nucleation. Neat PVDF films majorly contain α phase PVDF and the transformation from α to electroactive β polymorph in PVDF is possible due to the incorporation of CONPs as well as the homogeneous dispersion of these CONPs in PVDF matrix. Therefore in this context it is meaningful to analyze the interaction between the copper oxide nanoparticles and the polymer which promotes the formation of electroactive β phase. Improvement of the electroactive β phase fraction may be occurred due to the strong interactions between the PVDF matrix and embedded nanoparticles [8-9,24]. This type of ion-dipole interaction between the PVDF matrix and the loaded ferrite nanoparticles to form the electroactive β phase has also been reported by P. Martin et al. [32]. During the synthesis period of copper oxide nanoparticles we maintain the pH of the copper precursor solution at 13 by the use of NaOH solution. The variation of the Zeta potential of the copper oxide nanoparticles with pH of the respective precursor solution has been reported by H.B. Hassan et al. [33]. This variation of Zeta potential confirms that the surface of the as synthesized copper oxide nanoparticles are negatively charged. When the negatively charged nanoparticles are added to the PVDF matrix in the solution phase, the nanoparticles will act as the substrate for the formation of electroactive β phase. The partially positive $-CH_2$ dipoles of PVDF chains experience strong electrostatic interactions with the negatively charged

nanoparticle surfaces. The interaction leads to the alignment of the stabilized PVDF chains on the surface of the nanoparticles in a longer 'all-trans' (TTT) conformation resulting in the formation of electroactive β phase. Thus the surface of the nanoparticles acts as the nucleation center for the formation of the electroactive β phase. Fig. 14 depicts the schematic of the ion-dipole interaction mechanism between the nanoparticles and the polymer chains leading to the formation of electroactive β phase. It is worthwhile to mention here that our experimental observations show the presence of a small fraction of the electroactive γ phase of PVDF for the loaded PVDF films. Similar results have also been reported by A. C. Lopes et.al. for aluminosilicate/PVDF composites [34-36]. This γ phase formation may occur due to gauge effect which may be developed by the easier local internal chain rotation.

4. Conclusion:

In this work, a series of flexible CONPs/PVDF composite films were synthesized by a simple solution casting technique and the effect of CONPs on the polymorphism of PVDF is rigorously studied. The hexagonal copper oxide nanoparticles having average size of 60 nm were synthesized by the modified hydrothermal method. Our study confirms the successful inclusion of the well dispersed copper oxide nanoparticles in the PVDF matrix. XRD, FESEM, FTIR and thermal analyses of the composites films confirm that the loading of copper oxide nanoparticles in PVDF leads to the successful transformation from α to electroactive β polymorph in PVDF. β phase fraction in PVDF increases with increasing CONPs loading in polymer matrix. PCO5 shows highest β phase fraction c.a. 90%. The enhancement in β phase fraction of PVDF is attributed to the interaction of the negatively charged nanoparticles surfaces and the positive –CH2 group of the PVDF polymer chain, which leads to the alignment of the stabilized, longer 'all-trans' (TTT) conformation of PVDF chain on the surface of the nanoparticles resulting in the

nucleation of electroactive β phase. The calculated nanoparticles/polymer interface is also maximum for PCO5. The highest rate of enhancement (with nanofiller loading) in β phase fraction and nanoparticles/polymer interface values is observed for the 1wt% CONPs loaded PVDF composite film, however the values are further enhanced with increasing CONPs filler content in PVDF matrix. This indicates that the CONPs are nicely dispersed in PVDF matrix up to 5 wt% loading. The FESEM micrographs show that the size of the spherulites is decreased for the CONPs loaded PVDF films in comparison to the neat PVDF, which is facilitated due to the faster nucleation kinetics in PVDF due the presence of homogeneously dispersed CONPs nucleating agent. This phenomenon is also supported by the DSC result. Faster nucleation kinetics helps to enhance β polymorph in nanoparticles loaded PVDF. Thermal stability of the composites films are not degraded with the CONPs loading, rather the melting temperature is increased by ~3 °C for PCO5 in comparison to neat PVDF. In this context it should be noted that, the copper oxide nanoparticles are synthesized by simple, cost effective and environmentally benign hydrothermal method. Thus the as synthesized copper oxide nanoparticles loaded PVDF films with significantly enhanced β phase fraction may be used in future cost effective, efficient piezoelectric devices.

Acknowledgement:

The authors wants to acknowledge DST INSPIRE, Government of India (IF140204, IF140209) for the financial support and Dr. Sukhen Das for providing different characterization facilities.

References:

1. Q. M. Zhang, V. Bharti and X. Zhao, Science, 1998, **280(5372)**, 2101-2104.
2. S. Bauer, J. Appl. Phys.,1996, **80 (10)**, 5531-5558.
3. Q. M. Zhang, H. F. Li, M. Poh, H. S. Xu, Z.-Y. Cheng, F. Xia and C. Huang, Nature, 2002, **419**, 284-287.
4. S. Nambiar, J. T.W. Yeow, Biosensors and Bioelectronics, 2011, **26**, 1825–1832.
5. S. C. Mathur, J. I. Scheinbeim, B.A. Newman., J. Appl. Phys.,1984,**56**,2419–2425.
6. D. J. Bryan, J. B. Tang, S. A. Doherty, D. D. Hile, D. J Trantolo, D. L. Wise, I. C. Summerhayes, Journal of Neural Engineering, 2004, **1**, 91–98.
7. L. Huang, X. Zhuang, J. Hu, L. Lang, P. Zhang, Y. Wang, X. Chen, Y. Wei, X. Jing., Biomacromolecules, 2008,**9**,850–858.
8. E. Kar, N. Bose, S. Das, N. Mukherjee,S. Mukherjee, Phys.Chem.Chem.Phys, 2015, **17**, 22784-22798.
9. P. Thakur, A. Kool, B. Bagchi, N. A. Hoque, S. Das, P. Nandy, RSC Adv., 2015, **5**, 62819-62827.
10. P. Xu, K. Ye, M. Du et al., RSC Adv., 2015,**5**, 36656-36664.
11. P. Martins, M. Silva, S. L. Mendez, Nanoscale, 2015, **7**, 9457-9461.
12. H. Fang, Q. Li, W. He, J. Li, Q. Xue, C. Xu et al., Nanoscale, 2015, Advance Article.
13. Y. Yuan, Z. Xiao, B. Yang and J. Huang, J. Mater. Chem. A, 2014, **2**, 6027-6041.
14. P. Martins, A.C. Lopes, S. Lanceros-Mendez, Progress in Polymer Science, 2014, **39**, 683–706.
15. Y. Lu, J. Claude, B. Neese, Q. Zhang and Q. Wang, J. AM. CHEM. SOC., 2006, **128**, 8120-8121.

16. N. Karawasa , W. A. Goddard III, Macromolecules, 1992, **25**, 7268–7281.

17. V. Tomer, E. Manias, and C. A. Randall, J. Appl. Phys., 2011,**110**, 044107-10.

18. D. Mandal, K. Henkel, D. Schmeißer, Materials Letters, 2012, **73**, 123–125.

19. D. Mandal, K. Henkel and Dieter Schmeisser, J. Phys. Chem. B, 2011, **115**, 10567–10569.

20. A. B. da Silva, M. Arjmand, U.Sundararaj, R. E. S. Bretas, Polymer, 2014, **55**, 226-234.

21. S. M. Lebedev, O. S. Gefle , S. N. Tkachenko, J. Electrost., 2010, **68**, 122–127.

22. C. Putson, L. Lebrun, D. Guyomar, N. Muensit, P.J. Cottinet, L. Seveyrat and B. Guiffard., , J. Appl. Phys.,2011, **109**, 024104-8.

23. P. Thakur, A. Kool, B.Bagchi, S. Das, P.Nandy, Applied Clay Science, 2014, **99,** 149–159.

24. P. Thakur, A. Kool, B. Bagchi, S. Das, P. Nandy, Phys.Chem.Chem.Phys., 2015, **17**, 1368-1378.

25. D. Bhadra, Md. G. Masud, S. K. Deand, B. K .Chaudhuri, J. Phys. D: Appl. Phys. 2012, **45**, 485002.

26. J. S. Lee, K-Y Shin, C. Kim, J. Jang, Chem. Commun., 2013, **49**, 11047-11049.

27. N. Bose, M.Basu, S. Mukherjee, Materials Research Bulletin, 2012, **47**, 1368–1373.

28. M. Sharma, G. Madras , S.Bose, Cryst. Growth Des. 2015, **15**, 3345−3355.

29. Y. Abboud, T. Saffaj, A. Chagraoui, A. E. Bouari, K. Brouzi, O. Tanane , B. Ihssane, Appl. Nanosci. , 2014, **4**, 571–576.

30. S-H Park, W-J Lee, Scientific Reports, 2015, **5**, 09754.

31. A. Chafidz, M. Kaavessina, S. Al-Zahrani , M. N. Al-Otaibi, J. Polym. Res., 2014, **21**, 483.

32. P. Martins, C. M. Costa, M. Benelmekki, G. Botelhob , S. L. Mendez, Cryst. Eng .Comm, 2012, **14**, 2807.

33. H. B. Hassan , Z. Abdel Hamid, Int. J. Electrochem. Sci., 2011, **6**, 5741 – 5758.

34. A. Catarina Lopes, I. Correia Neves and S. Lanceros Mendez, Journal of Physical Chemistry C, 2015, **119 (9)**, 5211-5217.

35. A. C. Lopes, C. M. Costa, C. J. Tavares, I. C. Neves, and S. Lanceros-Mendez, J. Phys. Chem. C, 2011, **115 (37)**, 18076–18082.

36. A. C. Lopes, C. Caparros, S. Ferdov and S. Lanceros-Mendez, J Mater Sci, 2013, **48**, 2199–2206.

37. P. Martins, C. M. Costa, M. Benelmekki, G. Botelho, S. Lanceros-Me´ndez, J Mater Sci., 2013, **48**, 2681–2689.

List of Figure Captions

Figure 1: X-ray diffraction pattern of the hydrothermally synthesized copper oxide nanoparticles.

Figure 2: (a) FESEM image of the synthesized copper oxide nanoparticles. Inset shows the size distribution curve of the copper oxide nanoparticles; (b) TEM image of the synthesized copper oxide nanoparticles. Inset shows the size distribution curve of the copper oxide nanoparticles; (c) SAED pattern of the synthesized copper oxide nanoparticles; (d) EDAX result of the as synthesized copper oxide nanoparticles.

Figure 3: UV-Visible absorption spectrum of the as synthesized copper oxide nanoparticles.

Figure 4: (a) X-ray diffraction patterns of the neat PVDF (P0) and CONPs loaded PVDF films (PCO1, PCO3, PCO5); (b) Ratio of intensities at 20.6° and 18.2° of the samples P0, PCO1, PCO3, PCO5.

Figure 5: FESEM micrograph of the Neat PVDF film. Red circle shows the spherulite.

Figure 6: (a) FESEM micrograph of the CONPs loaded PVDF film (PCO5) at low magnification. Red circles show the spherulites; (b) FESEM micrograph of the sample PCO5 at high magnification; (c) EDAX analysis of the sample PCO5.

Figure 7: UV-Visible absorption results of neat PVDF (P0) and the CONPs loaded PVDF films (PCO1, PCO3 and PCO5).

Figure 8: (a) FTIR spectra of the P0 and CONPs loaded PVDF films (PCO1, PCO3 and PCO5). Dotted red and black lines are corresponding to the β phase and α phase PVDF respectively; (b) Variation of β phase fraction (F(β)) with CONPs loading in PVDF matrix.

Figure 9: (a) DTA of the samples P0, PCO1 and PCO5. Inset shows enlarged view of the DTA curve in the temperature range 140-175 °C; (b) TGA thermographs of the samples P0, PCO1 and PCO5. Inset shows the TGA thermographs of the synthesized copper oxide nanoparticles.

Figure 10: Coast-Redfern plot of (a) P0; (b) PCO1; (c) PCO5.

Figure 11: Variation of nanoparticle/polymer interface (m_I) with CONPs content.

Figure 12: DSC heating cycles for the samples (a) P0; (b) PCO1; (c) PCO5. DSC curves are fitted with multiple Gaussian functions corresponding to the α, β and γ phase PVDF.

Figure 13: DSC cooling cycle for the samples P0, PCO1 and PCO5.

Figure 14: Schematic of β phase formation mechanism.

Table-1. Activation energy at the major degradation region (around T_{max}) for the as synthesized samples.

Name of the sample	Maximum degradation temperature (T_{max}) (^{0}C)	Activation energy at the major degradation region (E^d) (KJoule/mole)	Regression factor (R^2)
P0	478.7	545.64	0.9998
PCO1	480.9	628.41	0.9997
PCO5	477.7	654.22	0.9995

Table-2. Melting temperature of the neat and CONP loaded PVDF films containing three different phases α, β, γ.

Sample Name	Melting Temperature of α –PVDF $(T_m)_\alpha$ (°C)	Melting Temperature of β –PVDF $(T_m)_\beta$ (°C)	Melting Temperature of γ –PVDF $(T_m)_\gamma$ (°C)
P0	156.0	161.5	164.6
PCO1	158.3	162.8	166.7
PCO5	153.5	162.4	166.9

Table-3 Crystallization temperature (T_c), enthalpy of crystallization (ΔH_c) and degree crystallinity (X_c) of the neat and CONPs loaded PVDF films.

Sample Name	Crystallization temperature (T_c)(°C)	Enthalpy (ΔH_c)	Crystallinity (X_c) (%)
P0	134.6	36.9	35
PCO1	136.0	34.8	33
PCO5	136.8	26.7	26

Figure 1

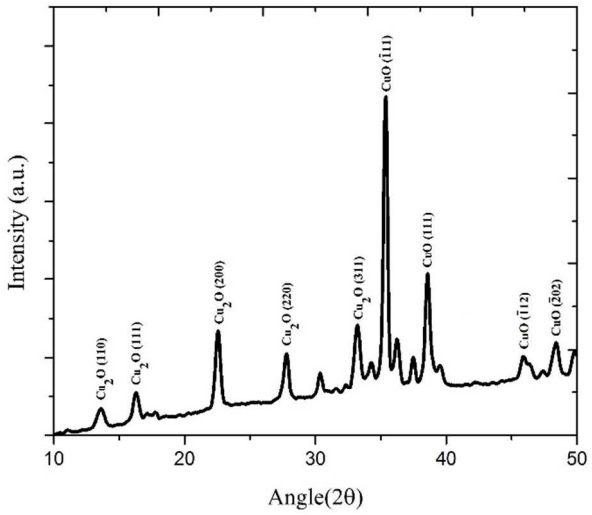

Figure 1: X-ray diffraction pattern of the hydrothermally synthesized copper oxide nanoparticles.

Figure 2a

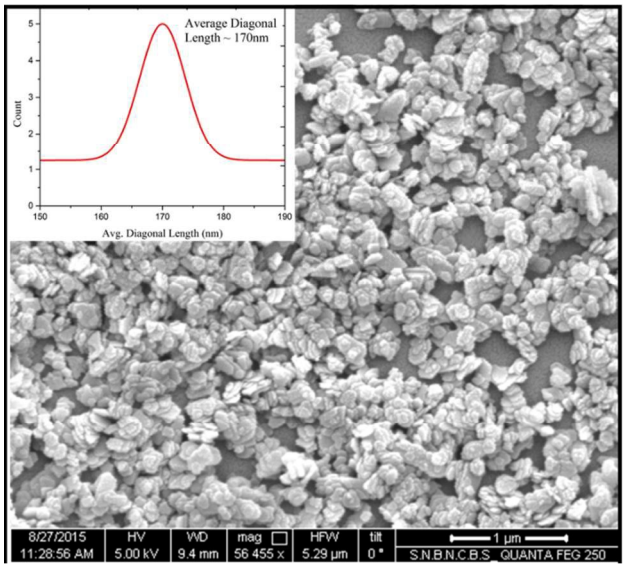

Figure 2b

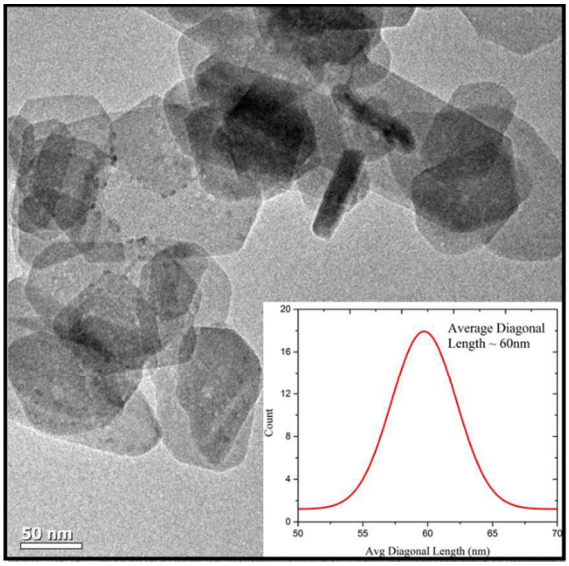

Figure 2c **Figure 2d**

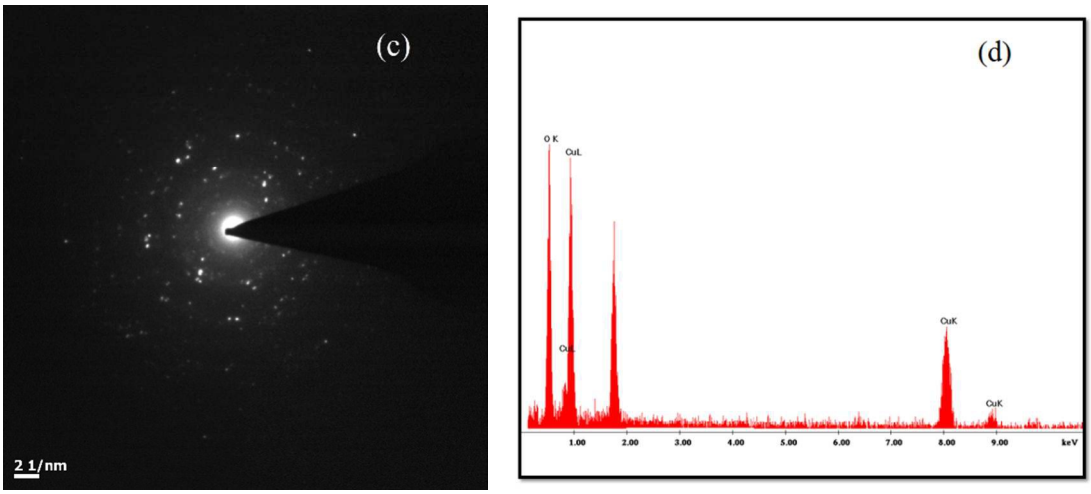

Figure 2: (a) FESEM image of the synthesized copper oxide nanoparticles. Inset shows the size distribution curve of the copper oxide nanoparticles; (b) TEM image of the synthesized copper oxide nanoparticles. Inset shows the size distribution curve of the copper oxide nanoparticles; (c) SAED pattern of the synthesized copper oxide nanoparticles; (d) EDAX result of the as synthesized copper oxide nanoparticles.

Figure 3

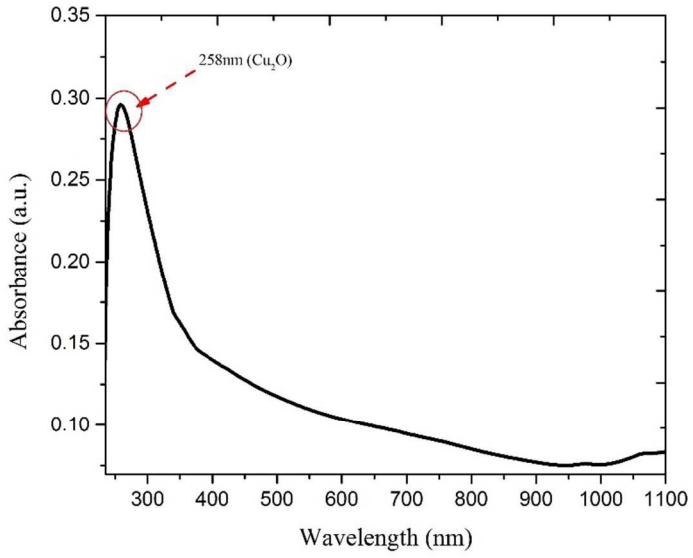

Figure 3: UV-Visible absorption spectrum of the as synthesized copper oxide nanoparticles.

Figure 4a-b

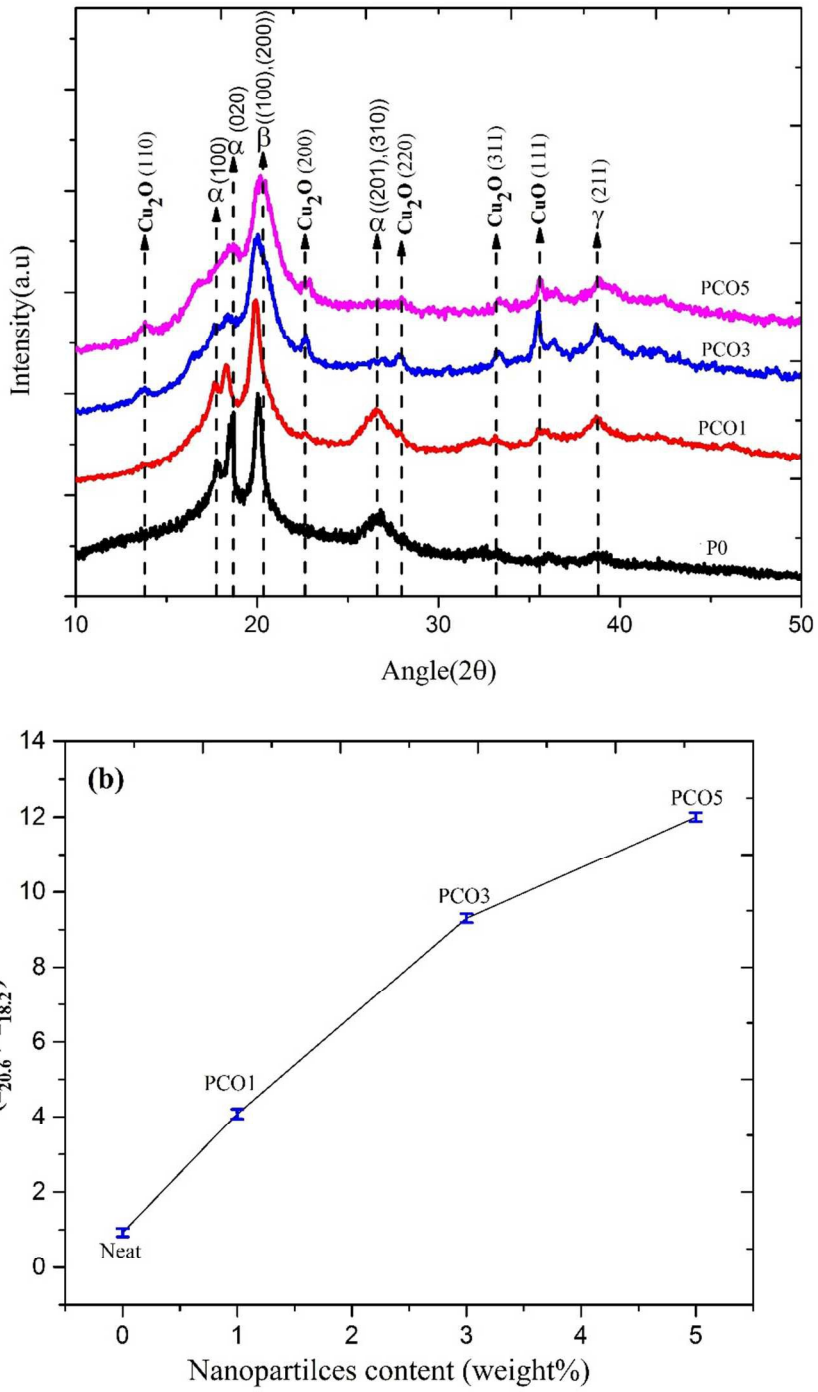

Figure 4: (a) X-ray diffraction patterns of the neat PVDF (P0) and CONPs loaded PVDF films (PCO1, PCO3, PCO5); (b) Ratio of intensities at 20.6° and 18.2° of the samples P0, PCO1, PCO3, and PCO5.

Figure 5

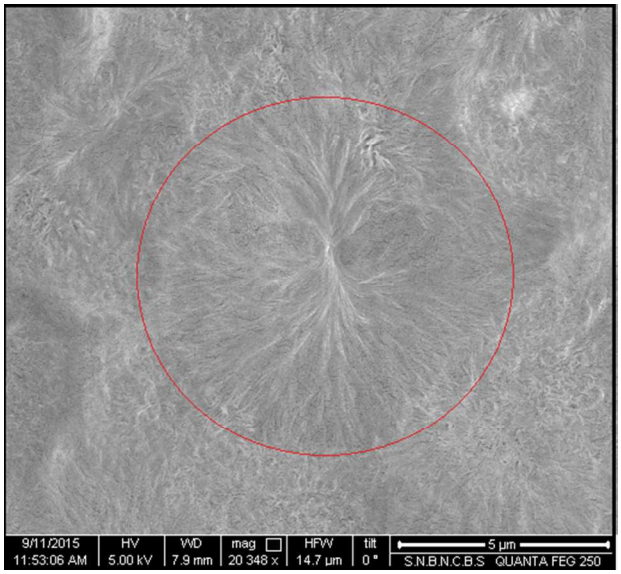

Figure 5: FESEM micrograph of the Neat PVDF film. Red circle shows the spherulite.

Figure 6a **Figure 6b**

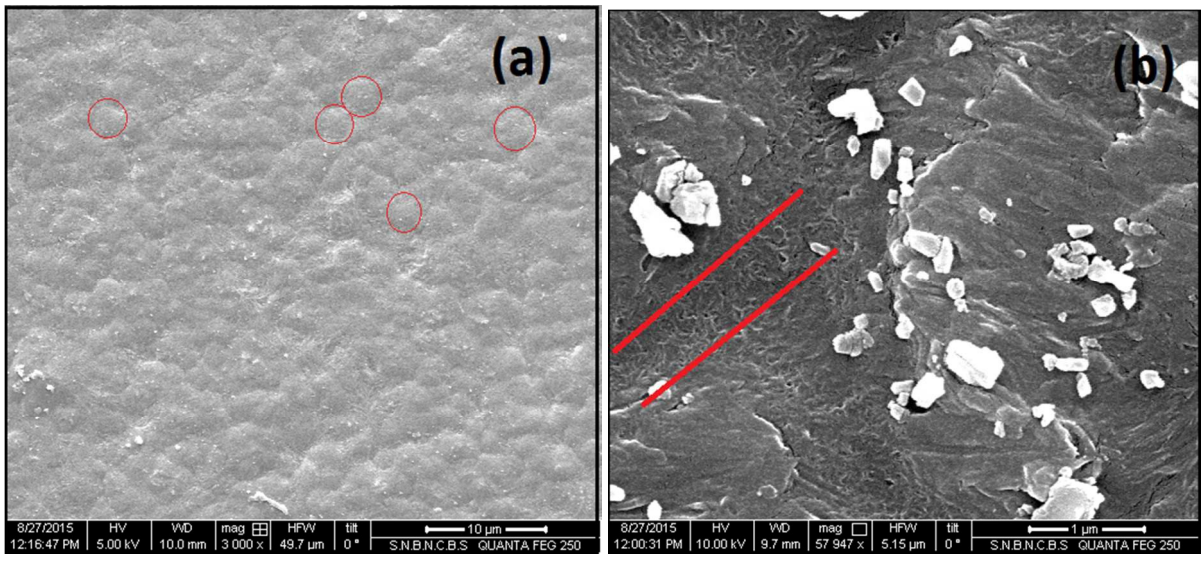

Figure 6c

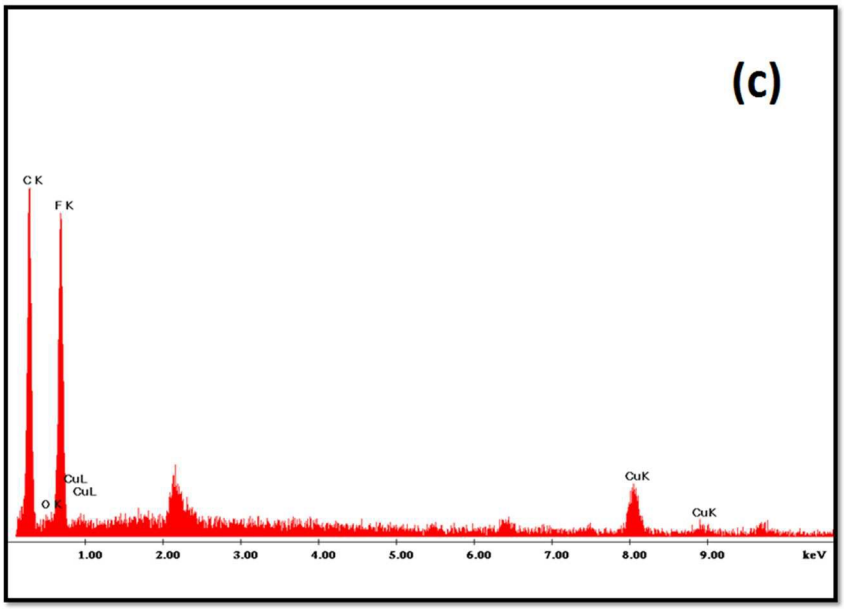

Figure 6: (a) FESEM micrograph of the CONPs loaded PVDF film (PCO5) at low magnification. Red circles show the spherulites; (b) FESEM micrograph of the sample PCO5 at high magnification; (c) EDAX analysis of the sample PCO5.

Figure 7

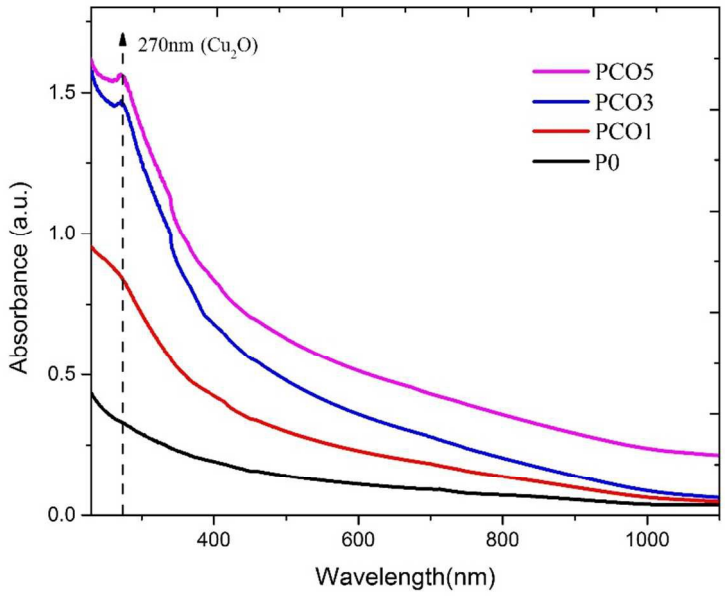

Figure 7: UV-Visible absorption results of neat PVDF (P0) and the CONPs loaded PVDF films (PCO1, PCO3 and PCO5).

Figure 8a

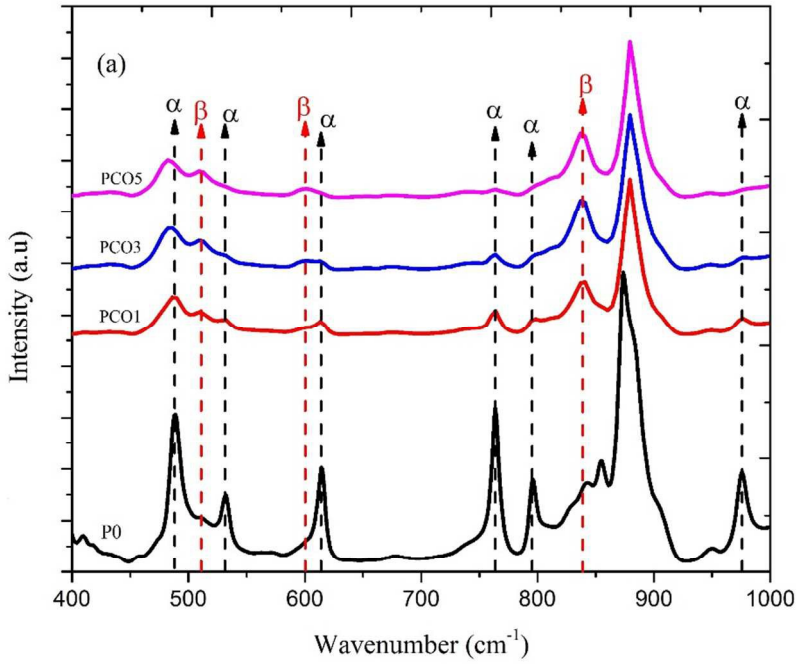

Figure 8b

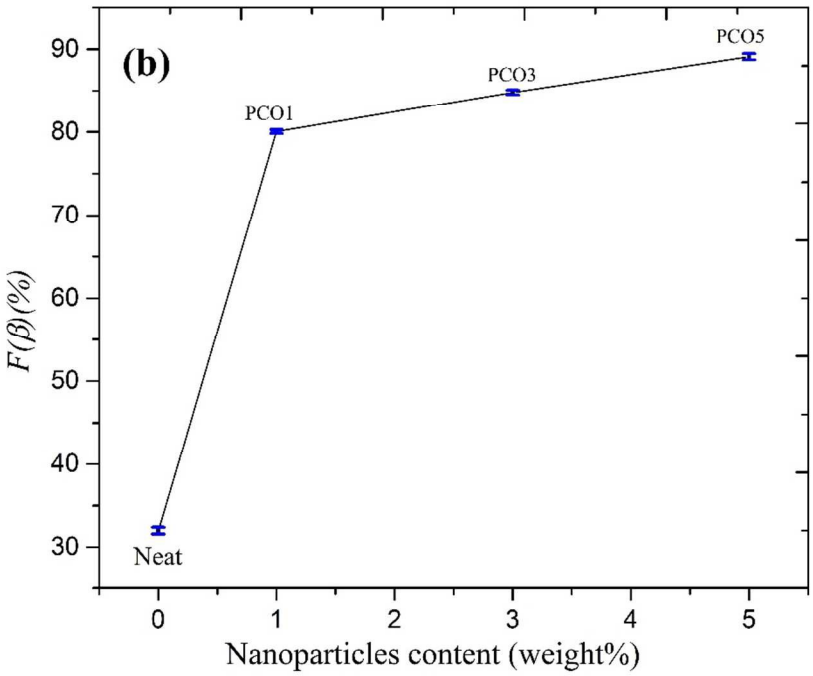

Figure 8: (a) FTIR spectra of the P0 and CONPs loaded PVDF films (PCO1, PCO3 and PCO5). Dotted red and black lines are corresponding to the β phase and α phase PVDF respectively; (b) Variation of β phase fraction (F(β)) with CONPs loading in PVDF matrix.

Figure 9a

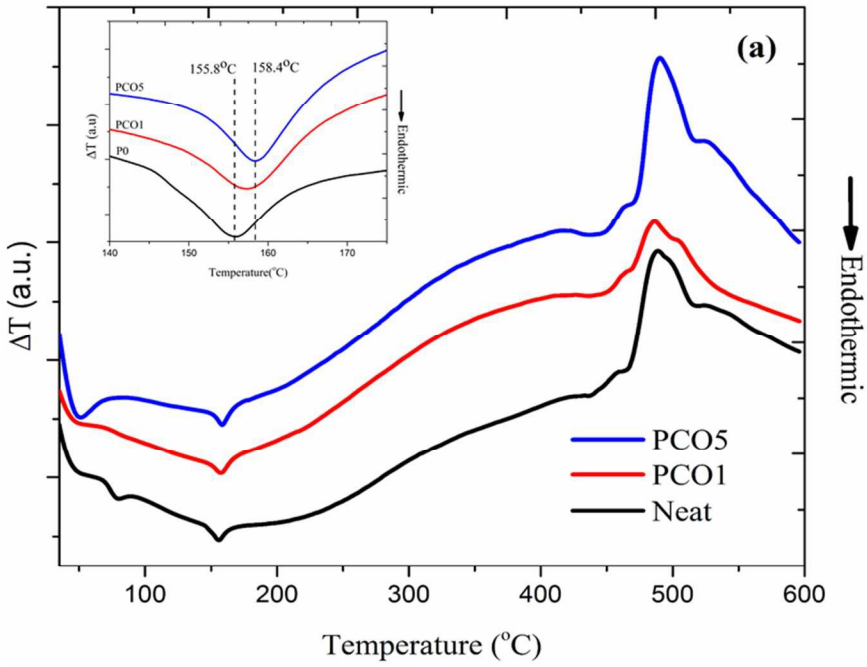

Figure 9b

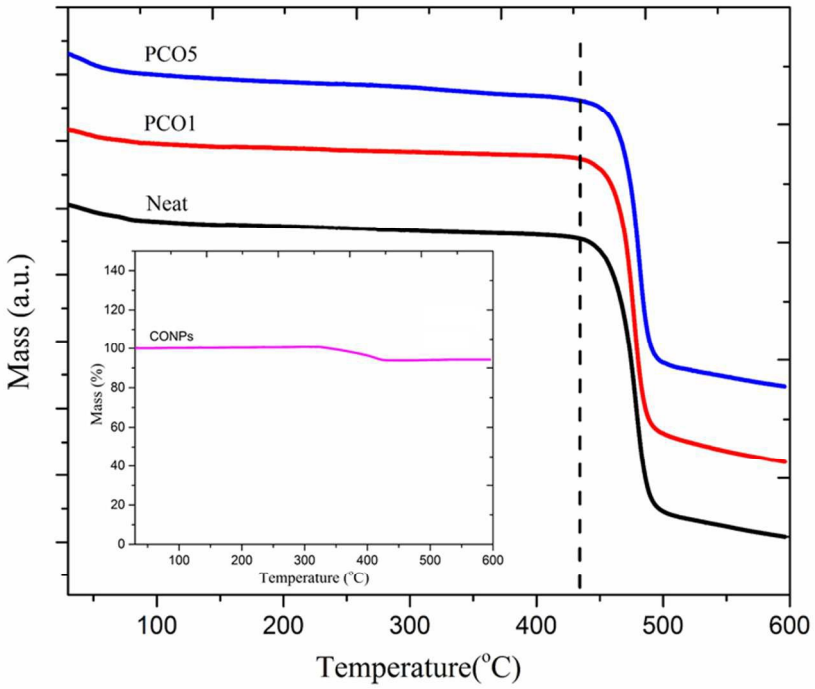

Figure 9: (a) DTA of the samples P0, PCO1 and PCO5. Inset shows enlarged view of the DTA curve in the temperature range 140-175 °C; (b) TGA thermographs of the samples P0, PCO1 and PCO5. Inset shows the TGA thermographs of the synthesized copper oxide nanoparticles.

Figure 10a

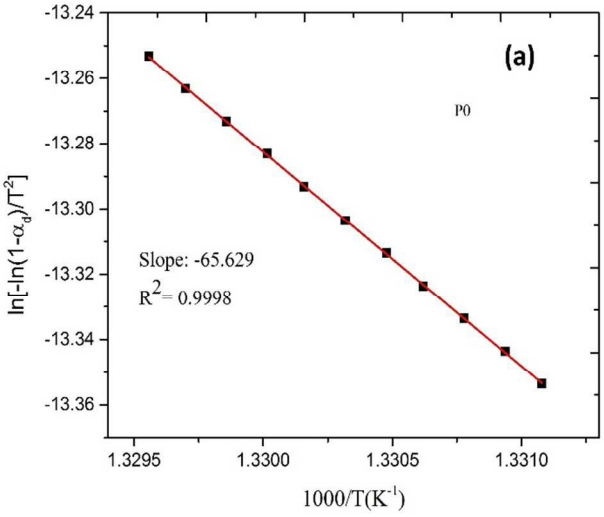

Figure 10b

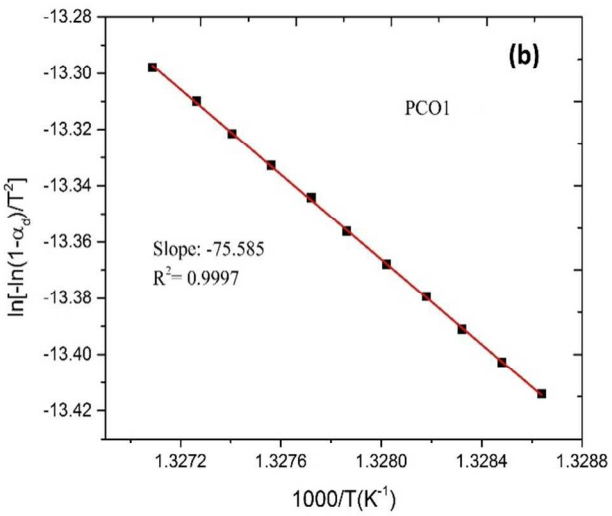

Figure 10c

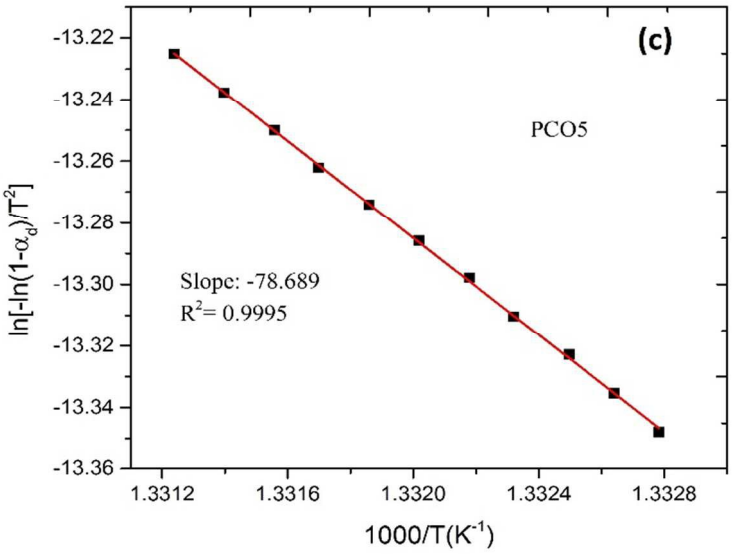

Figure 10: Coast-Redfern plot of (a) P0; (b) PCO1; (c) PCO5

Figure 11

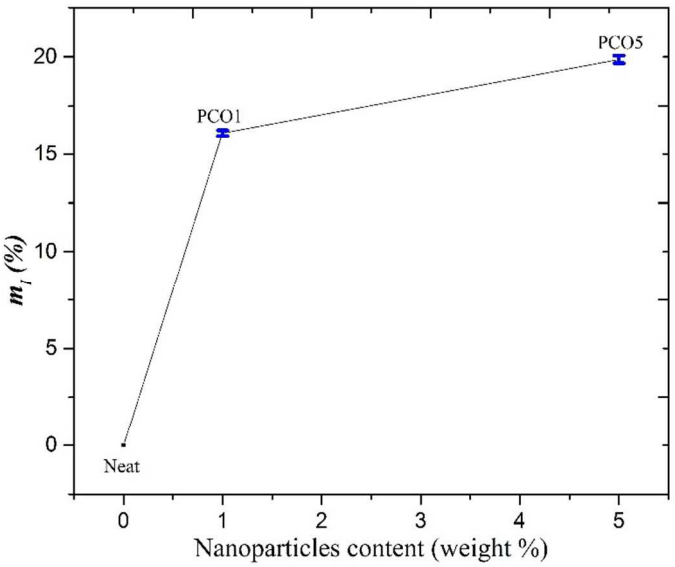

Figure 11: Variation of nanoparticle/polymer interface (m_I) with CONPs content.

Figure 12a

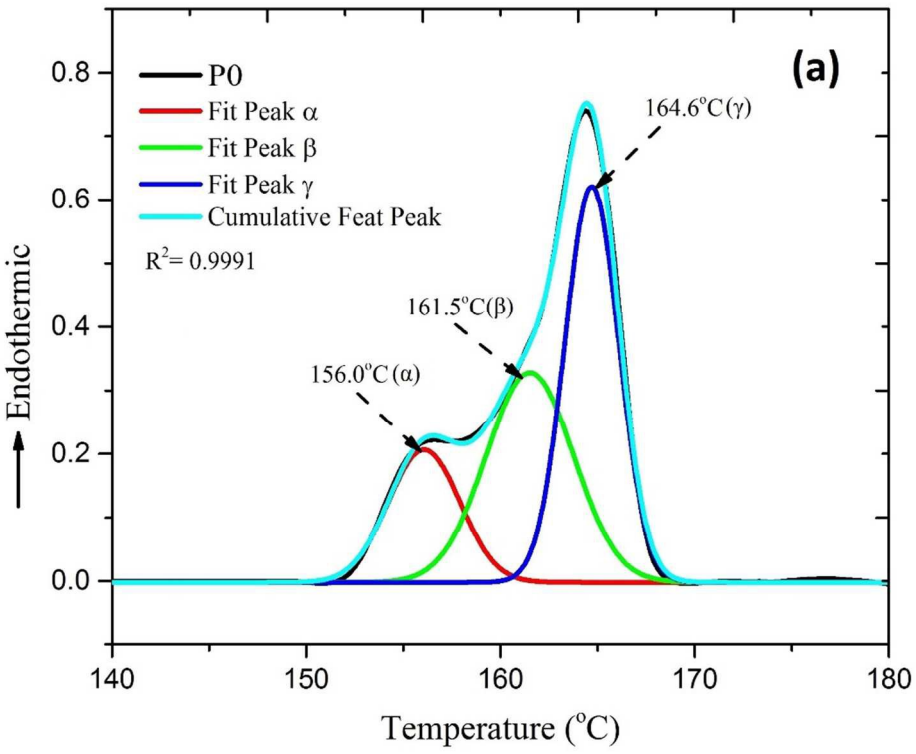

Figure 12b

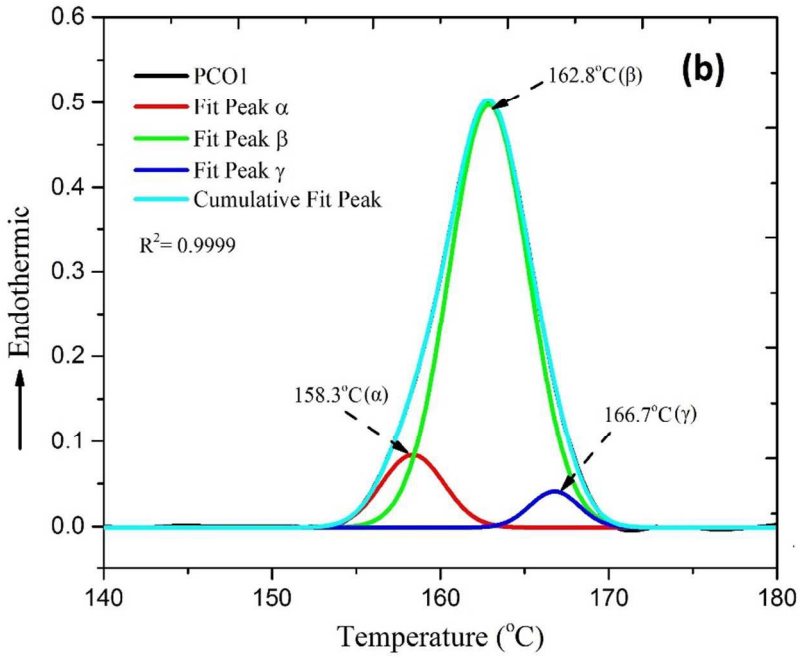

Figure 12c

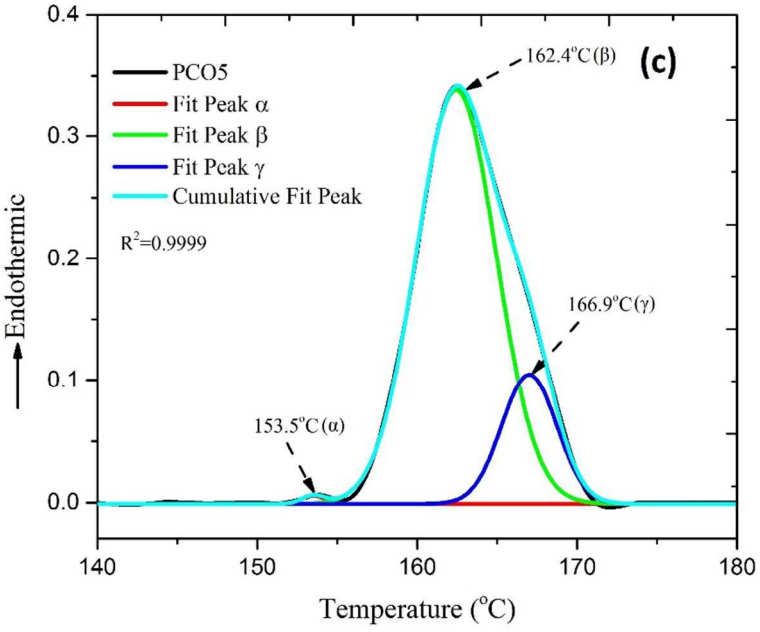

Figure 12: DSC heating cycles for the samples (a) P0; (b) PCO1; (c) PCO5. DSC curves are fitted with multiple Gaussian functions corresponding to the α, β and γ phase PVDF.

Figure 13

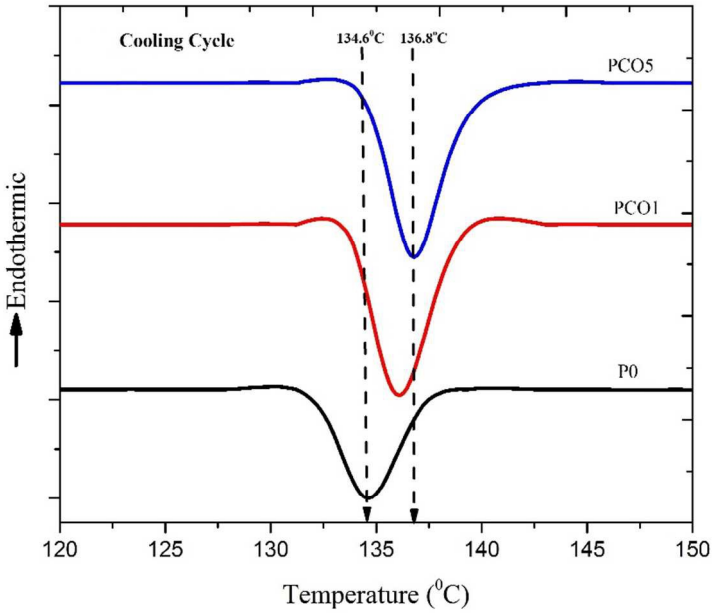

Figure 13: DSC cooling cycle for the samples P0, PCO1 and PCO5.

Figure 14

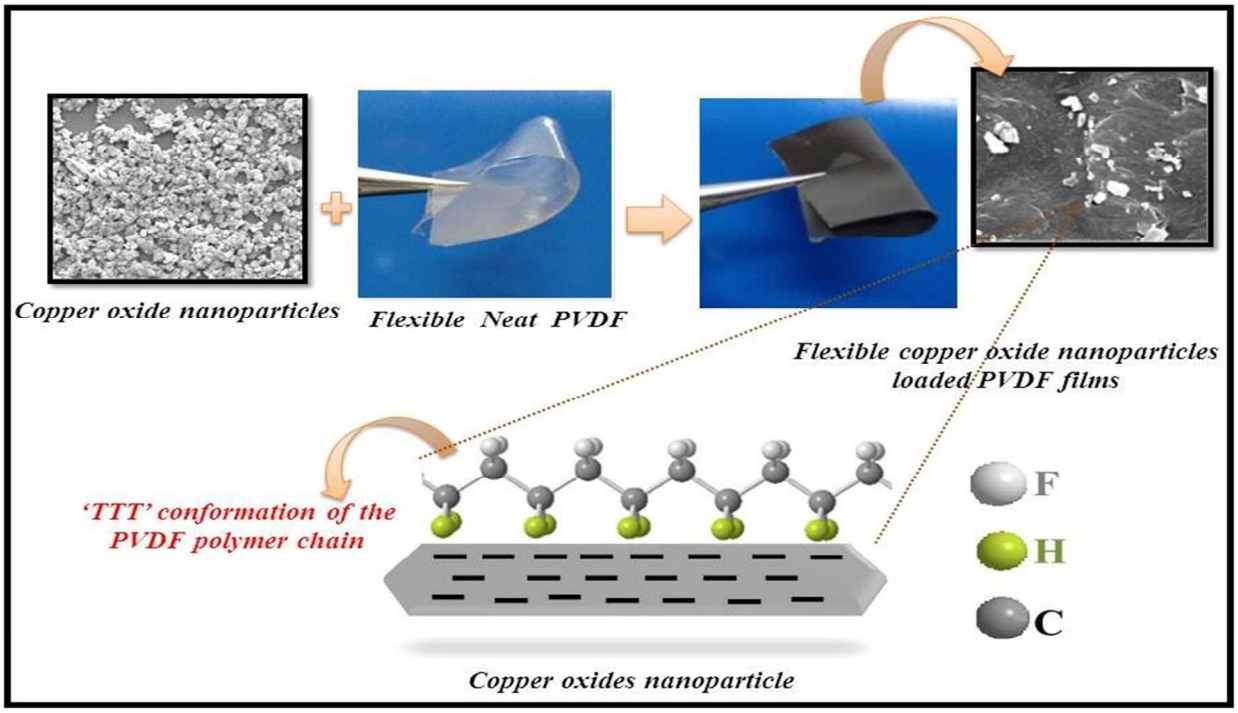

Figure 14: Schematic of β phase formation mechanism.

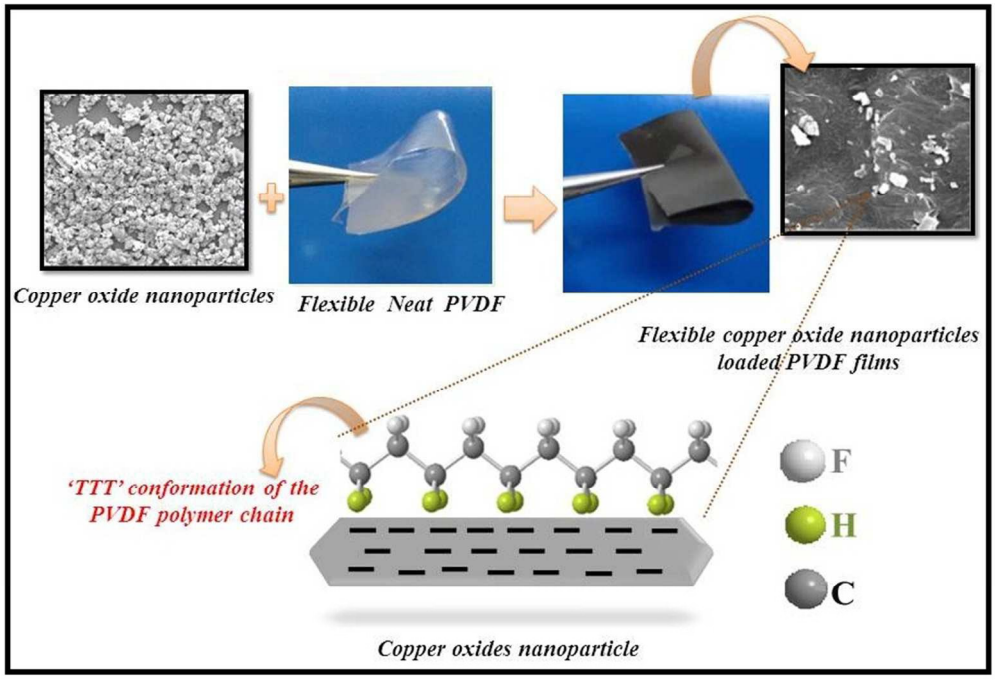

243x166mm (96 x 96 DPI)